ELECTROMAGNETIC DESIGN AND ANALYSIS OF MAGNETLESS DOUBLE-ROTOR DUAL-MODE MACHINES

Christopher H. T. Lee[*], K. T. Chau, and Chunhua Liu

Department of Electrical and Electronic Engineering, The University of Hong Kong, Pokfulam, Hong Kong, China

Abstract—Two magnetless double-rotor (DR) dual-mode machines, namely the DR DC-excited multi-tooth switched reluctance (DR-DC-MSR) machine and the DR flux-switching DC (DR-FS-DC) machine, are proposed for special direct-drive applications where two rotating bodies are required to operate independently. Both machines can offer two different operation modes, namely the doubly-salient DC (DSDC) mode and MSR mode, normal and fault-tolerant operations, respectively. With the independent armature windings, both machines are able to couple their two rotors with two rotating bodies operating at various speeds. The proposed machines are designed and analyzed by using the time-stepping finite element method (TS-FEM). The simulation results confirm the validity of the proposed machines.

1. INTRODUCTION

There is an accelerating pace on the development of electric vehicles (EVs) and renewable energy (RE) due to the increasing demands on the protection of the environment. In order to increase the market penetration of EVs and RE, the corresponding electric machines have to offer high efficiency, high power density, high controllability, wide speed range, and maintenance-free operation [1–3]. Over the years, the single-rotor permanent magnet (PM) machine has been actively developed to achieve these goals [4–6]. Nevertheless, because of the highly fluctuating price and supply of PM materials, the development of magnetless machines for EV motors and RE generators has attracted wide attention in recent years [7].

Recently, with the increasing application of two rotating loads, the double-rotor (DR) machine has been gaining more and more

attention. For example, the two different rotors of the DR machines can be separately connected to the wheels of the EVs to offer the electronic differential control [8]. In addition, the two rotors can perform the power split of the internal combustion engine to offer the energy optimization for hybrid EVs [9]. Recently, the flux-modulated PM (FMPM) machine which utilizes the magnetic-gearing effect has also employed the DR topology to perform low-speed high-torque propulsion [10]. For RE application, a DR contra-rotating generator has been proposed for wind power generation [11].

Compared with the PM machines, the magnetless machines generally suffer from lower torque density. In order to resolve this deficiency, the multi-tooth switched reluctance (MSR) machine which is favorable for high-torque operation has been proposed [12, 13]. With the employment of DC-field excitation, the DC-MSR machine can naturally offer the dual-mode operation [14]. On the other hand, by selecting a suitable combination of stator and rotor pole numbers with an appropriate DC-field excitation arrangement, the flux-switching DC (FS-DC) has been proposed [15]. Similar to the FS-PM machine, the FS-DC machine can exhibit the bipolar flux-linkage feature, thus improving the power density [16, 17].

In this paper, after purposely incorporating the DC-MSR and FS-DC topologies into the DR structure, the DR-DC-MSR and DR-FS-DC machines are newly proposed, for special direct-drive applications with two independent motoring wheels of EVs or for wind power generation with two sets of independently driven wind blades. By utilizing the controllable DC-field winding, the proposed machines can operate with two different modes, namely the doubly-salient DC (DSDC) mode and the MSR operation mode. In addition, the air-gap flux density of these two machines can readily be regulated for efficiency optimization. By applying the time-stepping finite element method (TS-FEM), the machines will be designed and analyzed for direct-drive applications where two rotating bodies are required to operate independently.

2. MACHINE DESIGN

By adopting the DR topology, the inner space of the proposed machines, namely the DR-DC-MSR and DR-FS-DC, are utilized to accommodate the inner rotor, hence boosting up the torque density. Without using any PM materials, the proposed machines take the definite merit of low cost.
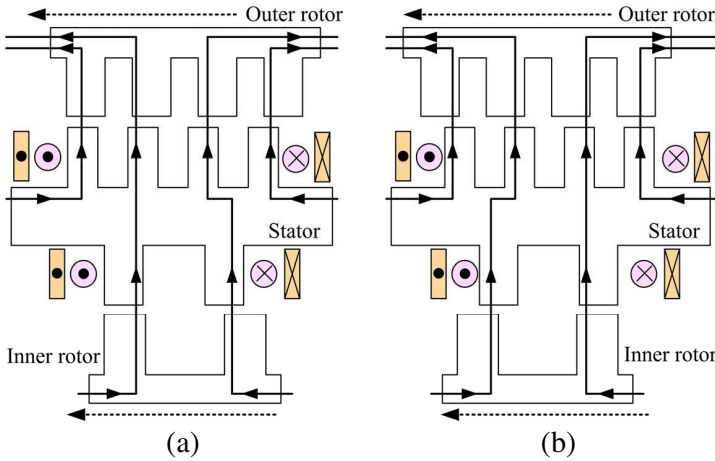
2.1. DR-DC-MSR Machine

Figure 1(a) shows the topology of the proposed DR-DC-MSR machine which consists of one stator sandwiched between the two rotors. With
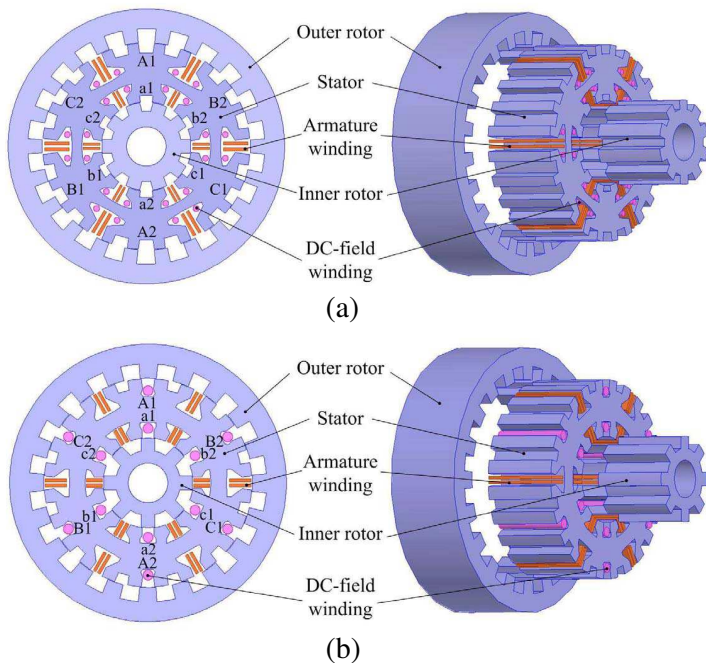
Figure 1. Proposed machines: (a) DR-DC-MSR, (b) DR-FS-DC.

the multi-tooth stator pole structure, it can offer the flux-modulation effect to boost up its torque density. Since the outer segment of the machine has a larger circumferential cross-sectional area, it generally adopts a larger number of rotor poles; meanwhile, the inner segment has a smaller number of rotor poles. For the outer segment, the stator consists of 6 salient poles, each having 4 teeth, thus resulting in an equivalence of 24 stator teeth. This complies with the outer rotor of 22 salient poles. Meanwhile, for the inner segment, the stator consists of 6 salient poles, each with 2 teeth, thus resulting in an equivalence of 12 stator teeth. This complies with the inner rotor of 10 salient poles.

The proposed DR-DC-MSR machine is equipped with two different sets of windings, namely the armature winding and DC-field winding. Both of them adopt the concentrated winding arrangement in such a way that two sets of windings are installed with their magnetic axes parallel each other. With this winding arrangement, the DC flux-linkages of both rotors flow with the same direction as shown in Figure 2. When the outer and inner armature windings are separately controlled, the outer rotor speed and the inner rotor speed can be regulated independently. Even when the armature windings are

Figure 2. DC flux-linkage paths of DR-DC-MSR machine: (a) Position 1, (b) Position 2.

connected in series, the two rotors can be operated together in the same direction. In addition, it can be seen that at different positions of the rotor poles, such as the Position 1 and Position 2 shown in Figure 2, the polarity of the DC flux-linkage remains the same.

The design of the pole-pair arrangement of this DR-DS-MSR machine is governed by the following criteria:

$$\begin{cases} N_{sp} = 2mi \\ N_{se} = N_{sp}N_{st} \\ N_r = N_{se} \pm 2i \end{cases} \tag{1}$$

where N_{sp} is the number of stator poles, N_{st} the number of stator teeth, N_{se} the number of equivalent stator poles, N_r the number of rotor poles, m the number of armature phases, and i is any integer. For the outer segment, by selecting $N_{sp} = 6$, $N_{st} = 4$ and $i = 1$, this ends up with $N_{se} = 24$ and $N_r = 22$; meanwhile, for the inner segment, $N_{sp} = 6$, $N_{st} = 2$ and $i = 1$, this ends up with $N_{se} = 12$ and $N_r = 10$. These come up with the proposed structure of the DR-DC-MSR machine.

2.2. DR-FS-DC Machine

Figure 1(b) shows the topology of the DR-FS-DC machine which has a similar design procedure as the DR-DS-MSR machine. For the outer segment of the machine, the stator consists of 6 salient poles, each

with 4 teeth, thus resulting in an equivalence of 24 stator teeth. This complies with the outer rotor of 20 salient poles. Meanwhile, for the inner segment, the stator consists of 6 salient poles, each with 2 teeth, thus resulting in an equivalence of 12 stator teeth. This complies with the inner rotor of 8 salient poles.

Compared with the DR-DC-MSR machine, the DR-FS-DC machine also installs with two types of winding, but its armature winding adopts the concentrated winding arrangement while the DC-field winding adopts the toroidal arrangement. With this configuration, the two sets of windings are installed with their magnetic axes perpendicular each other. Since these two types of windings are located in different slots, the DR-FS-DC machine can accommodate more armature coils than its counterpart. In addition, as the two sets of windings are physically detached, the DR-FS-DC machine is more fault-tolerant to the inter-turn winding short-circuited fault [18] than the DR-DC-MSR machine in which both sets of windings are bundled together. With the toroidal winding arrangement, the DC flux-linkages of two rotors flow in opposite directions as shown in Figure 3. Nevertheless, the two rotors can be operated in the same direction when the armature windings are independently controlled. In addition, it can be seen that along with the movement of the rotor poles, as depicted in Position 1 and Position 2 in Figure 3, the polarity of the DC flux-linkage reverses, hence offering the flux-switching feature that the iron core is better utilized.
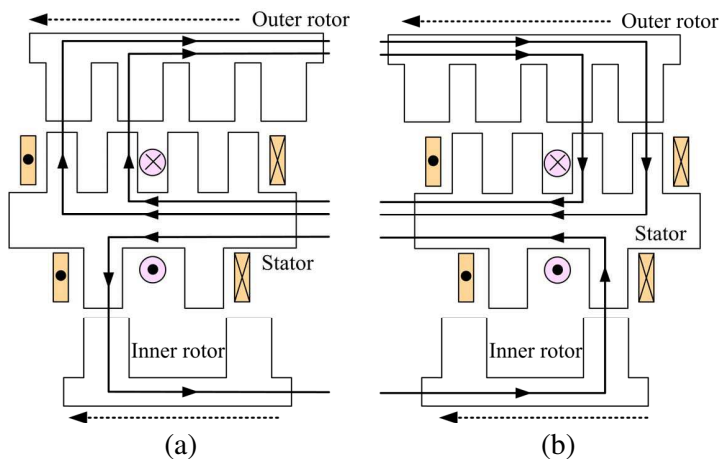
Figure 3. DC flux-linkage paths of DR-FS-DC machine: (a) Position 1, (b) Position 2.

The design of the pole-pair arrangement of this DR-FS-DC machine is based on the following criteria [16]:

$$\begin{cases} N_{sp} = 2mi \\ N_{se} = N_{sp}N_{st} \\ N_r = N_{se} - N_{sp} \pm 2i \end{cases} \tag{2}$$

For the outer segment, by selecting $N_{sp} = 6$, $N_{st} = 4$ and $i = 1$, it ends up with $N_{se} = 24$ and $N_r = 20$; meanwhile, for the inner segment, when $N_{sp} = 6$, $N_{st} = 2$ and $i = 1$, this ends up with $N_{se} = 12$ and $N_r = 8$. These come up with the proposed structure for DR-FS-DC machine.

To have a fair comparison between the two proposed machines, the stator diameter, rotor diameter, air-gap length, stack length, number of equivalent stator poles and number of armature phases are set to be the same. The corresponding key design data are tabulated in Table 1.

Table 1. Key data of proposed machines.

Item	DR-DC-MSR	DR-FS-DC
Outer rotor outside diameter	280.0 mm	280.0 mm
Outer rotor inside diameter	211.2 mm	211.2 mm
Stator outside diameter	210.0 mm	210.0 mm
Stator inside diameter	91.2 mm	91.2 mm
Inner rotor outside diameter	90.0 mm	90.0 mm
Inner rotor inside diameter	40.0 mm	40.0 mm
Air-gap length of both segments	0.6 mm	0.6 mm
Stack length	80.0 mm	80.0 mm
No. of stator poles of both segments	6	6
No. of stator teeth of outer segment	4	4
No. of stator teeth of inner segment	2	2
No. of equivalent stator poles of outer segment	24	24
No. of equivalent stator poles of inner segment	12	12
No. of rotor poles of outer segment	22	20
No. of rotor poles of inner segment	10	8
No. of armature phases	3	3
No. of turns per outer armature coil	50	65
No. of turns per inner armature coil	40	55

3. OPERATION PRINCIPLE

With the addition of DC-field excitation, the proposed machines can be operated at two different operation modes, namely the DSDC and MSR modes. The DSDC mode mainly serves for normal operation, whereas the MSR mode is devoted to fault-tolerant operation. It should be noted that fault-tolerant operation of electric machines is very important for EVs. For instance, an EV may cause traffic jam or even fatal accident when the machine is suddenly malfunction under fault. The proposed machines can provide fault-tolerant operation (namely the MSR mode) which enables the EV to continue running when there is a fault in the DC-field winding.

3.1. DSDC Mode

When the DC-field winding is excited, the proposed two machines can be operated by using the bipolar conduction scheme which is similar to the conventional doubly salient PM (DSPM) machine operation [19, 20]. When the DC flux-linkage Ψ_{DSDC} is increasing and the no-load EMF becomes positive, a positive armature current I_{BLDC} is applied to produce a positive torque T_{DSDC}. Similarly, a negative armature current $-I_{\mathrm{BLDC}}$ is applied when the Ψ_{DSDC} is decreasing and the no-load EMF is negative, hence also producing a positive torque. This operation mode is known as the DSDC mode and the operating waveforms are shown in Figure 4(a). Each phase performs $120°$ conduction with $\theta_2 - \theta_1 = \theta_4 - \theta_3 = 120°$. The resulting electromagnetic torque T_{DSDC} can be expressed as:

$$T_{\mathrm{DSDC}} = \frac{1}{2\pi} \int_0^{2\pi} \left(i_{\mathrm{BLDC}} \frac{d\psi_{\mathrm{DSDC}}}{d\theta} + \frac{1}{2} i_{\mathrm{BLDC}}^2 \frac{dL_D}{d\theta} \right) d\theta \qquad (3)$$
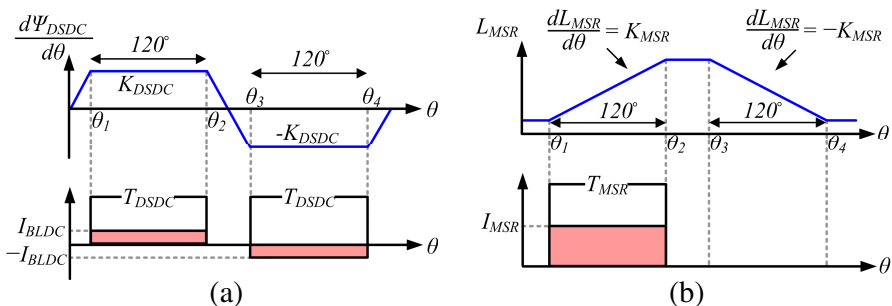

Figure 4. Operation principles: (a) DSDC mode, (b) MSR mode.

where L_D is the self-inductance. Under this mode, the torque is mainly contributed by the DC-field torque component, whereas the reluctance torque component is small and pulsates with a zero average value. Hence, after neglecting the pulsation torque component, the torque expression can be written as:

$$
T_{\mathrm{DSDC}} = \frac{1}{2\pi} \left(\int\limits_{\theta_1}^{\theta_2} I_{\mathrm{BLDC}} K_{\mathrm{DSDC}} d\theta + \int\limits_{\theta_3}^{\theta_4} (-I_{\mathrm{BLDC}}) (-K_{\mathrm{DSDC}}) \, d\theta \right)
$$
$$
= \frac{2}{3} I_{\mathrm{BLDC}} K_{\mathrm{DSDC}} \tag{4}
$$

and K_{DSDC} is the slope of Ψ_{DSDC} with respect to θ.

Similar to the conventional DSPM machines, the DR-DC-MSR and DR-FS-DC machines adopt the same speed control strategy. The operating speed is governed by the value of N_r and the operating frequency as given by [13]:

$$
\omega = \frac{60 f_{\mathrm{PH}}}{N_r} \tag{5}
$$

where ω is the rotor speed and f_{PH} the commutating frequency of a particular phase. Obviously, the value of N_r of the outer segment of the proposed machines is larger than that of its inner segment. Thus, the outer rotor of the proposed machines is operated at lower speed while achieving higher torque when the armature windings are under the same operating frequency.

3.2. MSR Mode

Whilst the DC-field winding is under an open-circuit fault or short-circuit fault, the DC-field current will be cut off and the proposed machines can then be operated by using the unipolar conduction scheme. Namely, a unipolar rectangular current I_{MSR} is fed to the armature winding during the increasing period of the self-inductance L_{MSR} so that the corresponding reluctance torque T_{MSR} is positive within $\theta_2 - \theta_1 = 120°$ as shown in Figure 4(b). This mode is known as the MSR mode. However, at this mode, only half of the torque producing period is utilized, and thus the torque performance is degraded and the torque ripple is larger than that at the DSDC mode. Therefore, this mode is regarded as fault-tolerant operation [18, 21] when the DC-field winding is under fault condition. The reluctance torque at this MSR mode can be written as:

$$T_{\mathrm{MSR}} = \frac{1}{2\pi}\int_0^{2\pi}\left(\frac{1}{2}i_{\mathrm{MSR}}^2\frac{dL_{\mathrm{MSR}}}{d\theta}\right)d\theta = \frac{1}{2\pi}\int_{\theta_1}^{\theta_2}\left(\frac{1}{2}I_{\mathrm{MSR}}^2 K_{\mathrm{MSR}}\right)d\theta$$

$$= \frac{1}{6}I_{\mathrm{MSR}}^2 K_{\mathrm{MSR}} \tag{6}$$

where K_{MSR} is the slope of L_{MSR} with respect to θ. In order to maintain the same torque level at both modes, the Equations (4) and (6) should be equated to yield:

$$I_{\mathrm{MSR}} = 2\sqrt{\frac{I_{\mathrm{BLDC}}K_{\mathrm{DSDC}}}{K_{\mathrm{MSR}}}} \tag{7}$$

Based on Equation (7), the armature current at the MSR mode can be deduced, which enable the proposed machines to offer the same average torque as that at the DSDC mode. However, since the MSR mode generally requires a larger armature current and utilizes only half of the torque producing period, the corresponding efficiency and torque ripple are worse than that at the DSDC mode.

4. ELECTROMAGNETIC FIELD ANALYSIS

Electromagnetic field analysis has been widely adopted for the development of the electric machines, and it can be generally categorized as the analytical field calculation [22] and the numerical field calculation [23]. In this paper; the TS-FEM is employed for the analysis of the proposed machine performances. To describe the machine modeling, three sets of equations are established. First, the electromagnetic field equation is governed by [24, 25]:

$$\begin{cases} \Omega : \dfrac{\partial}{\partial x}\left(v\dfrac{\partial A}{\partial x}\right) + \dfrac{\partial}{\partial y}\left(v\dfrac{\partial A}{\partial y}\right) = -(J_z + J_f) \\ A|_S = 0 \end{cases} \tag{8}$$

where Ω is the field solution region, A and J_z the z-direction components of vector potential and current density, respectively, J_f the equivalent current density of the excitation field, S the Dirichlet boundary, and v the reluctivity. Second, the armature circuit equation of the machine during motoring is given by:

$$u = Ri + L_e\frac{di}{dt} + \frac{l}{s}\iint_{\Omega_e}\frac{\partial A}{\partial t}d\Omega \tag{9}$$

where u is the applied voltage, R the winding resistance, L_e the end winding inductance, l the axial length, s the conductor area of each turn of phase winding, and Ω_e the total cross-sectional area of conductors of each phase winding. On the contrary, the circuit equation during generation is given by:

$$u = \frac{l}{s} \iint_{\Omega_e} \frac{\partial A}{\partial t} d\Omega - Ri - L_e \frac{di}{dt} \qquad (10)$$

Third, the motion equation of the machine is given by:

$$J_m \frac{\partial \omega}{\partial t} = T_e - T_L - \lambda \omega \qquad (11)$$

where J_m is the moment of inertia, T_L the load torque and λ the damping coefficient. These three types of equations can be calculated at each time step; hence, the steady-state and transient performances of the proposed machine can be deduced. The magnetic solver performing the finite element analysis for the proposed machines is the JMAG-Designer. Figure 5 shows the generated meshes, and Figure 6 shows the corresponding no-load magnetic field distributions. Each simulation process takes a few hours based on a standard PC.

Figure 7 shows the no-load electromotive force (EMF) of the proposed machines at the rated speed versus the DC-field excitation. For fair comparison, both machines are operated under the same operating frequency of 200 Hz. It can be observed that both machines perform similarly and their no-load EMF increases with the DC-field excitation linearly before 700 A-turn at which magnetic saturation begins to occur. These validate that the proposed machines can strengthen or weaken the flux densities by regulating the DC-field currents in order to achieve the efficiency optimization. Meanwhile,

(a)   (b)
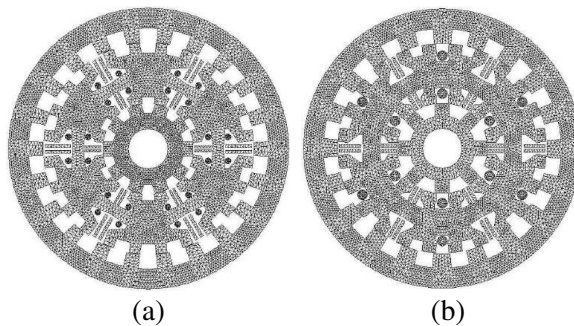
Figure 5. Generated meshes of FEM model: (a) DR-DC-MSR, (b) DR-FS-DC.

(a)   (b)
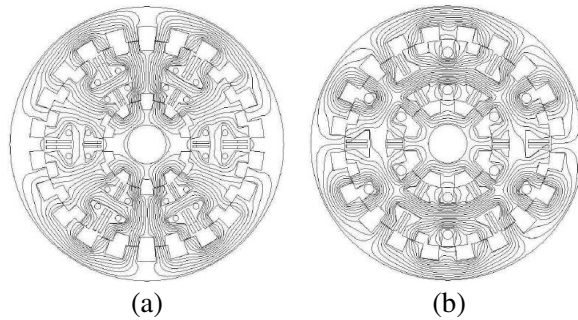
Figure 6. No-load magnetic field distributions: (a) DR-DC-MSR, (b) DR-FS-DC.


(a)   (b)
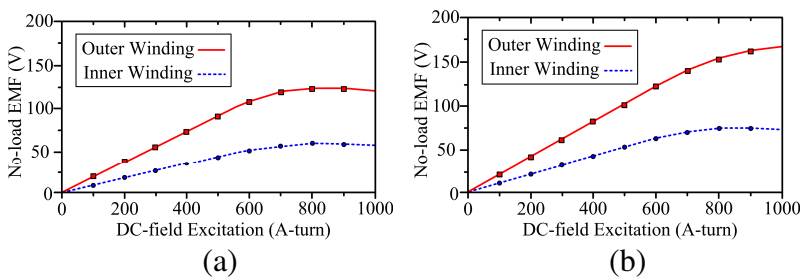
**Figure 7.** No-load EMF versus DC-field excitation characteristics: (a) DR-DC-MSR, (b) DR-FS-DC.

due to the flux-switching feature and better winding accommodation, the DR-FS-DC machine can offer larger no-load EMF without magnetic saturation as compared with its DR-DC-MSR counterpart.

Figure 8 shows the air-gap flux density waveforms of both machines under the no-load condition and the DC-field excitation is set at 700 A-turn. It can be observed that the peak values of these waveforms are essentially the same. It should also be noted that for both machines, the original flux of the outer segment of the stator pole is modulated into four portions in accordance with the number of teeth per stator pole; meanwhile, the inner segment of the stator pole is modulated into two portions instead. This verifies that the proposed machines can offer the flux-modulation effect to boost up the torque density accordingly.

Figures 9 and 10 show the DC flux-linkage waveforms at the DSDC mode (with the DC-field excitation of 700 A-turn) and the self-inductance waveforms at the MSR mode (without the DC-field excitation) of the proposed machines, respectively. As expected, the
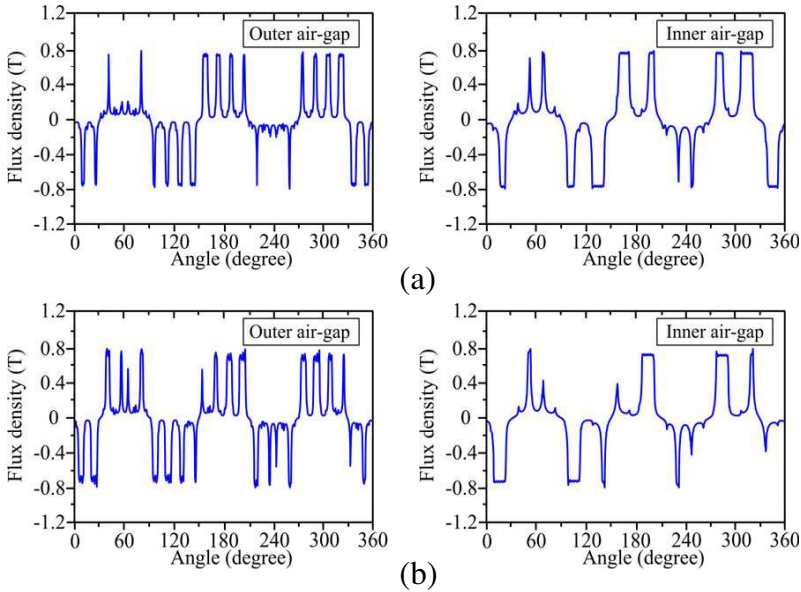
Figure 8. Air-gap flux density waveforms: (a) DR-DC-MSR, (b) DR-FS-DC.
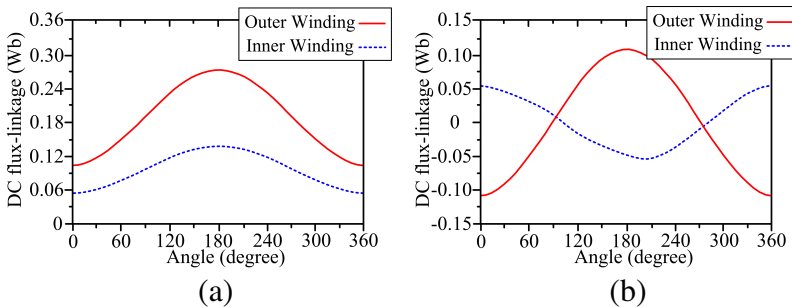
Figure 9. DC flux-linkage waveforms at DSDC mode: (a) DR-DC-MSR, (b) DR-FS-DC.

DC flux-linkages of the DR-DC-MSR machine shown in Figure 9(a) are unipolar in both windings, whereas the DC flux-linkages of the DR-FS-DC machine shown in Figure 9(b) are bipolar in both windings. It confirms that the DR-FS-DC machine can offer the flux-switching feature. On the other hand, it can be observed that the self-inductances of the DR-FS-DC machine shown in Figure 10(b) are larger than that of the DR-DC-MSR machine shown in Figure 10(a), which is due to the fact that the DR-FS-DC can accommodate larger number of windings.
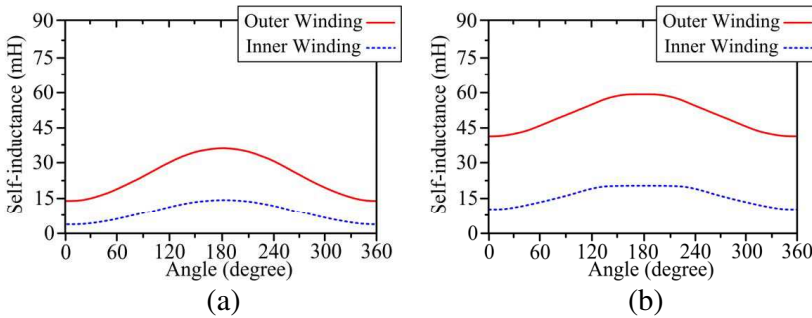
Figure 10. Self-inductance waveforms at MSR mode: (a) DR-DC-MSR, (b) DR-FS-DC.

In order to maintain the same torque level between the DSDC and MSR modes, the armature current at the MSR mode is given by Equation (7) in which the values of K_{DSDC}, and K_{MSR} can be deduced from Figures 9 and 10, respectively as summarized in Table 2.

**Table 2.** Key parameters at different modes.

Item	DR-DC-MSR		DR-FS-DC	
	Outer	Inner	Outer	Inner
Rated current at DSDC mode	5 A	5 A	5 A	5 A
Slope of DC flux-linkage K_{DSDC}	0.143/120	0.073/120	0.179/120	0.076/120
Slope of self-inductance K_{MSR}	0.021/120	0.008/120	0.018/120	0.009/120
Rated current at MSR mode	11.7 A	13.5 A	14.1 A	13.0 A

5. PERFORMANCE COMPARISON

By using the TS-FEM, the performances of the proposed machines can be thoroughly analyzed. Firstly, the no-load EMF waveforms of the DR-DC-MSR machine and DR-FS-DC machine are simulated as shown in Figure 11. The DR-DC-MSR machine can generate up to 121.3 V at the outer winding, and 53.4 V at the inner winding. Meanwhile, the DR-FS-DC machine can achieve up to 142.5 V at the outer winding, and 71.8 V at the inner winding. It can be seen that the no-load EMF waveforms of both machines have the balanced three-phase patterns. As expected, the outer and inner windings of the DR-DC-MSR machine have the same polarity, whereas the windings of the DR-FS-DC machine have the opposite polarities. It should be noted that the no-load EMF waveforms of the DR-FS-DC machine are
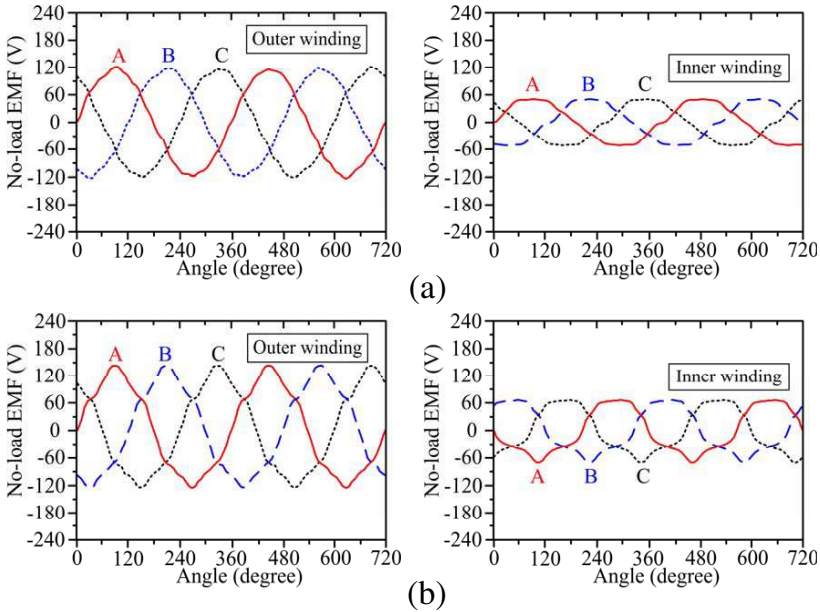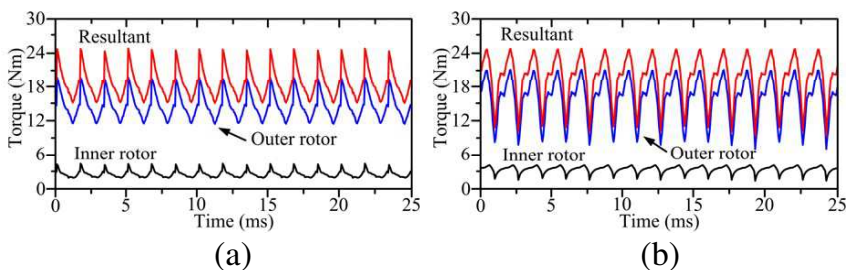
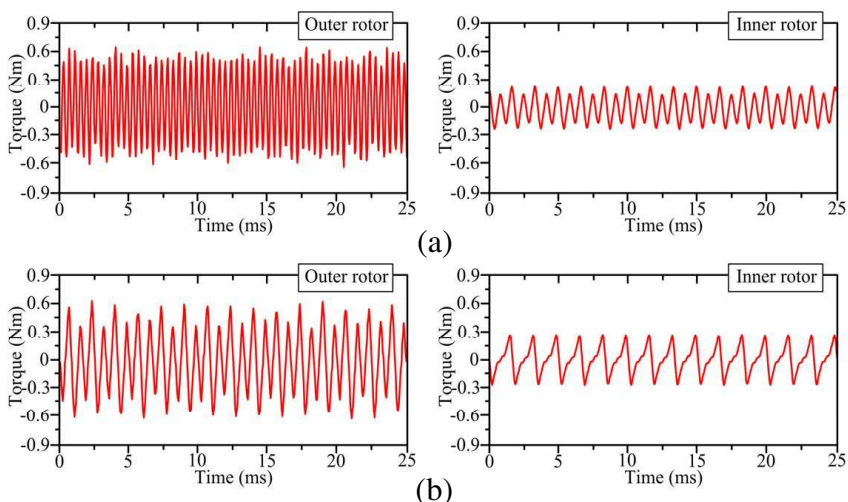**Figure 11.** No-load EMF waveforms: (a) DR-DC-MSR, (b) DR-FS-DC.
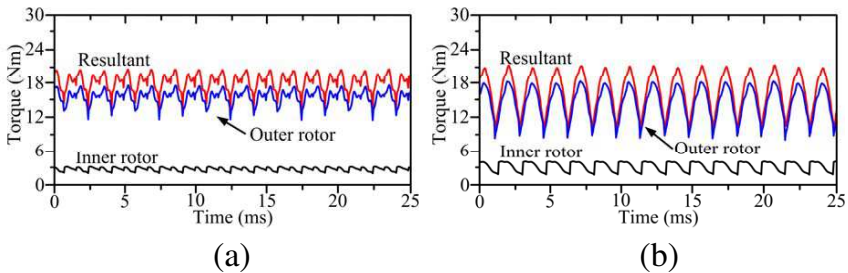
Figure 12. Torque waveforms of DR-DC-MSR machine: (a) DSDC mode, (b) MSR mode.

not very symmetrical, and this will end up with larger torque ripple production. The torque ripple problem can be remedied by applying the technique of injected-harmonic-current operation [26], but this is out of the scope of this paper.

Secondly, Figures 12 and 13 show the torque performances at steady state of the DR-DC-MSR machine and the DR-FS-DC machine, respectively. It can be observed that the average steady torques of the outer rotor, inner rotor and resultant torque of the DR-DC-

Figure 13. Torque waveforms of DR-FS-DC machine: (a) DSDC mode, (b) MSR mode.

Figure 14. Cogging torque waveforms: (a) DR-DC-MSR, (b) DR-FS-DC.

MSR machine at the DSDC mode are 14.9 Nm, 2.95 Nm and 17.9 Nm, respectively; meanwhile, at the MSR mode, they are 14.5 Nm, 2.72 Nm and 17.2 Nm, respectively. For the DR-FS-DC machine, its average steady torques of the outer rotor, inner rotor and resultant torque at the DSDC mode are 15.8 Nm, 3.17 Nm and 19.0 Nm, respectively; meanwhile, at the MSR mode, they are 15.6 Nm, 2.81 Nm and 18.4 Nm, respectively. These verify that both machines can offer the similar torque levels at the MSR mode as compared with that at the DSDC mode. It should also be noted that in order to operate both rotors of the DR-FS-DC machine in the same direction, the armature currents of both windings have to be controlled independently. In addition,

Table 3. Machine performance comparison.

Item	DR-DC-MSR		DR-FS-DC	
	DSDC	MSR	DSDC	MSR
Power	1220 W	1160 W	1480 W	1420 W
Operating frequency	200 Hz	200 Hz	200 Hz	200 Hz
Rated speed of outer rotor	545 rpm	545 rpm	600 rpm	600 rpm
Rated speed of inner rotor	1200 rpm	1200 rpm	1500 rpm	1500 rpm
No-load EMF of outer rotor	121.3 V	N/A	142.5 V	N/A
No-load EMF of inner rotor	53.4 V	N/A	71.8 V	N/A
Rated torque of outer rotor	14.9 Nm	14.5 Nm	15.8 Nm	15.6 Nm
Rated torque of inner rotor	2.95 Nm	2.72 Nm	3.17 Nm	2.81 Nm
Resultant rated torque	17.9 Nm	17.2 Nm	19.0 Nm	18.4 Nm
Torque density	3635 Nm/m^3	3493 Nm/m^3	3859 Nm/m^3	3737 Nm/m^3
Torque per current density	3.34 MNm^3/A	1.28MNm^3/A	3.42 MNm^3/A	1.22MNm^3/A
Rated efficiency	86.4%	68.2%	85.3%	65.8%
Torque ripple of outer rotor	35.1%	70.2%	58.2%	87.2%
Torque ripple of inner rotor	45.6%	74.6%	52.6%	91.6%
Torque ripple of resultant torque	36.3%	72.4%	57.3%	89.3%
Cogging torque of outer rotor	4.5%	N/A	4.1%	N/A
Cogging torque of inner rotor	6.4%	N/A	8.4%	N/A

the resultant torque densities of the DR-DC-MSR and DR-FS-DC machines are up to 3635 Nm/m^3 and 3859 Nm/m^3, respectively, which are comparable to that (3500–5500 Nm/m^3) of the conventional PM machines [2, 4]. Also, the corresponding values of torque per current density are up to 3.34 MNm^3/A and 3.42 MNm^3/A, respectively, which are comparable to though slightly lower than that (3.8–5.0 MNm^3/A) of the conventional PM machines [2, 4]. Consequently, the torque ripples of the DR-DC-MSR and DR-FS-DC machines at the DSDC mode can be found to be 36.3% and 57.3%, respectively; meanwhile, at the MSR mode, they are 72.4% and 89.3%, respectively. As expected, the torque ripples at the MSR mode are higher than that at the DSDC mode. Therefore, the MSR mode should be operated as the fault-tolerant mode when the DC-field excitation is under fault condition.

Finally, the cogging torque waveforms of both machines at the DSDC mode under the DC-field excitation of 700 A-turn are simulated as shown in Figure 14. It can be found that the peak values at the outer rotor and inner rotor of the DR-DC-MSR machine are 0.67 Nm and 0.19 Nm, respectively; meanwhile, for the DR-FS-DC machine, they are 0.65 Nm and 0.27 Nm, respectively. As compared with the rated torques, they are only 4.5% and 6.4% for the DR-DC-MSR machine and 4.1% and 8.4% for the DR-FS-DC machine, which are much lower than that of the DSPM machine [19].

6. CONCLUSION

In this paper, two magnetless DR machines, namely the DR-DC-MSR machine and DRFSDC machine, have been newly developed for special direct-drive applications such as motoring two independent wheels of EVs or serving for wind power generation using two sets of independently driven wind blades. Both machines can offer two different operation modes, namely the DSDC and MSR modes, for normal and fault-tolerant operations, respectively, hence improving the system reliability. The performances of both machines are thoroughly analyzed by the TS-FEM and their performances are summarized in Table 3. Between them, the DR-FS-DC machine offers better performances than the DR-DC-MSR counterpart, especially in terms of the torque density and power density. Meanwhile, as expected, both machines offer much better efficiencies in the DSDC mode than that in the MSR mode. It is anticipated that these two DR machines will have great potentials for EV propulsion and RE harvesting.

ACKNOWLEDGMENT

REFERENCES

1. Zhu, Z. Q. and D. Howe, "Electrical machines and drives for electric, hybrid and fuel cell vehicles," *Proceedings of IEEE*, Vol. 95, No. 4, 746–765, April 2007.

2. Chau, K.-T., W. Li, and C. H. T. Lee, "Challenges and opportunities of electric machines for renewable energy," *Progress In Electromagnetics Research B*, Vol. 42, 45–74, 2012.

3. Liu, C., K. T. Chau, and Z. Zhang, "Novel design of double-stator single-rotor magnetic-geared machines," *IEEE Transactions on Magnetics*, Vol. 48, No. 11, 4180–4183, November 2012.

4. Chau, K. T., C. C. Chan, and C. Liu, "Overview of permanent-magnet brushless drives for electric and hybrid electric vehicles," *IEEE Transactions on Industrial Electronics*, Vol. 55, No. 6, 2246–2257, June 2008.

5. Zhang, J., M. Cheng, Z. Chen, and W. Hua, "Comparison of stator-mounted permanent-magnet machines based on a general

power equation," *IEEE Transactions on Energy Conversion*, Vol. 24, No. 4, 826–834, December 2009.

6. Liu, C., K. T. Chau, J. Zhong, W. Li, and F. Li, "Quantitative comparison of double-stator permanent magnet vernier machines with and without HTS bulk," *IEEE Transactions on Applied Superconductivity*, Vol. 22, No. 3, 5202405, June 2012.

7. Zhu, Z. Q., "Switched flux permanent magnet machines — Innovation continues," *International Conference on Electrical Machines and Systems*, 1–10, August 2011.

8. Kawamura, A., N. Hoshi, T. W. Kim, T. Yokoyama, and T. Kume, "Analysis of anti-directional-twin-rotary motor drive characteristics for electric vehicles," *IEEE Transactions on Industrial Electronics*, Vol. 44, No. 1, 64–70, February 1997.

9. Hoeijmakers, M. J. and J. A. Ferreria, "The electric variable transmission," *IEEE Transactions on Industry Applications*, Vol. 42, No. 4, 1092–1100, July 2006.

10. Liu, C. and K.-T. Chau, "Electromagnetic design and analysis of double-rotor flux-modulated permanent-magnet machines," *Progress In Electromagnetics Research*, Vol. 131, 81–97, 2012.

11. Booker, J. D., P. H. Mellor, R. Wrobel, and D. Drury, "A compact, high efficiency contra-rotating generator suitable for wind turbines in the urban environment," *Renewable Energy*, Vol. 35, No. 9, 2027–2033, September 2010.

12. Faiz, J., J. W. Finch, and H. M. B. Metwally, "A novel switched reluctance motor with multiple teeth per stator pole and comparison of such motors," *Electric Power Systems Research*, Vol. 34, No. 3, 197–203, September 1995.

13. Lee, C. H. T., K. T. Chau, C. Liu, D. Wu, and S. Gao, "Quantitative comparison and analysis of magnetless machines with reluctance topologies," *IEEE Transactions on Magnetics*, Vol. 49, No. 7, 3969–3972, July 2013.

14. Lee, C. H. T., K. T. Chau, and C. Liu, "Design and analysis of a DC field multitooth switched reluctance machine by using soft-magnetic-composite material," *International Symposium on Industrial Electronics*, TD-001244, May 2013.

15. Wang, Y., J. Sun, Z. Zou, and K. T. Chau, "Design and analysis of a HTS flux-switching machine for wind energy conversion," *IEEE Transactions on Applied Superconductivity*, Vol. 23, No. 3, 5000904, June 2013.

16. Chen, J. T., Z. Q. Zhu, and D. Howe, "Stator and rotor pole combination for multi-tooth flux-switching permanent-magnet

brushless AC machines," *IEEE Transactions on Magnetics*, Vol. 44, No. 12, 4659–4667, December 2008.

17. Cao, R., C. Mi, and M. Cheng, "Quantitative comparison of flux-switching permanent-magnet motors with interior permanent magnet motor for EV, HEV, and PHEV applications," *IEEE Transactions on Magnetics*, Vol. 48, No. 8, 2374–2384, August 2012.

18. Yu, C. and K. T. Chau, "New fault-tolerant flux-mnemonic doubly-salient permanent-magnet motor drive," *IET Electric Power Application*, Vol. 5, No. 5, 393–403, December 2009.

19. Cheng, M., K. T. Chau, and C. C. Chan, "Static characteristics of a new doubly salient permanent magnet motor," *IEEE Transactions on Energy Conversion*, Vol. 16, No. 1, March 20–25, 2001

20. Liu, C., K. T. Chau, and J. Z. Jiang, "A permanent-magnet hybrid brushless integrated- starter-generator for hybrid electric vehicles," *IEEE Transactions on Industrial Electronics*, Vol. 57, No. 12, 4055–4064, December 2010.

21. Zhao, W., M. Cheng, W. Hua, H. Jia, and R. Cao, "Back-EMF harmonic analysis and fault-tolerant control of flux-switching permanent-magnet machine with redundancy," *IEEE Transactions on Industrial Electronics*, Vol. 58, No. 5, 1926–1935, May 2011.

22. Li, W. and K.-T. Chau, "Analytical field for linear tubular magnetic gears using equivalent anisotropic magnetic permeability," *Progress In Electromagnetics Research*, Vol. 127, 155–171, 2012.

23. Wang, Y., K. T. Chau, C. C. Chan, and J. Z. Zhang, "Transient analysis of a new outer-rotor permanent-magnet brushless dc drive using circuit-field-torque time-stepping finite element method," *IEEE Transactions on Magnetics*, Vol. 38, No. 2, 1297–1300, March 2002.

24. Salon, S. J., *Finite Element Analysis of Electrical Machines*, Kluwer Academic Publishers, Boston, USA, 1995.

25. Niu, S., S. L. Ho, W. N. Fu, and J. Zhu, "Eddy current reduction in high-speed machines and eddy current loss analysis with multislice time-stepping finite-element method," *IEEE Transaction on Magnetics*, Vol. 48, No. 2, 1007–1010, February 2012.

26. Zhao, W., M. Cheng, R. Cao, and J. Li, "Experimental comparison of remedial single-channel operations for redundant flux-switching permanent-magnet motor drive," *Progress In Electromagnetics Research*, Vol. 123, 189–204, 2012.